Received 31 October 2017; | Revised 07 March 2018; | Accepted XX

DOI: xxx/xxxx

RESEARCH ARTICLE

The effects of coherent structures on the global response of floating offshore wind turbines

Erin E. Bachynski*[1,2] | Lene Eliassen[1,3]

[1]Department of Marine Technology, Norwegian University of Science and Technology, Trondheim, Norway
[2]NTNU AMOS, Norwegian University of Science and Technology, Trondheim, Norway
[3]Ocean Engineering, SINTEF Ocean, Trondheim, Norway

Correspondence
*Erin E. Bachynski, Marine Technology Center, 7491 Trondheim, Norway. Email: erin.bachynski@ntnu.no

ABSTRACT

The global dynamic response of floating wind turbines is commonly simulated using aero-hydro-servo-elastic tools which consider numerically generated wind files as input. Based on the guidelines given in existing standards, two methods of generating such wind files are typically used: the Mann uniform shear model and the Kaimal spectral and exponential coherence model. Both models consider the Kaimal spectrum with similar frequency characteristics: the main difference between the approaches is related to the spatial coherence. The present work examines the consequences of using the two different wind file generation methods for estimating the global responses of representative spar, semi-submersible, and tension leg platform (TLP) 5 MW wind turbines. Predictions of the standard deviation of low-frequency responses in operational conditions, including motions at the natural frequency in surge and pitch as well as quasi-static (spar, TLP) and resonant (semi-submersible) motions in yaw, are seen to differ up to 30-40 % depending on the wind field model. The differences in motion responses have important consequences for the design of the mooring system components. Proper orthogonal decomposition (POD) techniques are used to qualitatively explain the differing spatial coherence of the wind field. Simulations including a limited number of POD modes in the wind field highlight the importance of the low-frequency, energy-rich modes, suggesting that this type of visualization can be a useful tool.

KEYWORDS:
floating wind turbine, turbulence model, coherence, mooring system, proper orthogonal decomposition

1 | INTRODUCTION

Floating wind turbines (FWTs) are a relatively new technology, and provide a feasible means of generating electricity from the abundant wind resource in deep (> 50 m) water.

Numerical simulation tools for global dynamic analysis of FWTs, known as aero-hydro-servo-elastic design tools (1), have been developed by numerous research groups. Significant efforts are underway to compare, validate, and improve these tools (2, 3), such that designers can use them to develop more cost-efficient and reliable FWTs. The assessment of global responses, such as the global platform motions, bending moments in the tower, or mooring line tensions, is typically carried out for a wide variety of design load conditions (DLCs). Several design standards prescribe sets of DLCs which should be considered in order to evaluate cyclic and extreme loads on structural components.

The environmental input for each DLC includes wave parameters (significant wave height, peak period, and spectral form) as well as wind parameters (mean wind speed, shear profile, turbulence intensity, and wind spectra). Time-domain realizations of the wave elevation are typically generated using an inverse FFT, where the amplitude and phase of the Fourier components are drawn from Rayleigh and uniform distributions, respectively (4). Hydrodynamic loads are then computed based on an appropriate model (such as Morison's equation for slender elements, or first or second order potential theory for large-volume FWTs). Three-dimensional turbulent wind fields which cover the rotor (accounting for the probable motions of the FWT) must also be generated as input for each DLC, such that aerodynamic loads can be computed using blade element/momentum or generalized dynamic wake methods.

Existing design standards (5, 6) for FWTs refer to the IEC-61400-1 standard (7), which suggests two possible models for generating time-varying numerical wind fields:

1. the Mann uniform shear model (here called "Mann"), or
2. the Kaimal spectral and exponential coherence model (here called "Kaimal").

While the frequency content of the two models should be identical (following the Kaimal spectrum), there are important differences in spatial coherence between the two approaches, as described in greater detail in Section 2. Furthermore, there may be significant differences in the resulting spectra depending on whether site-specific or generic turbulence parameters (such as the length scale L and anisotropy parameter Γ) are used (8). The present work does not address which of these methods gives a better representation of real wind inflow - such conclusions would require extensive measurement data which are not available - but rather focuses on the differences in response predictions based on these models. Based on a single month of measurement, the vertical coherence at the FINO1 platform seems to be more similar to the Mann turbulence model than to the Kaimal wind field (9), but more comprehensive measurements are needed.

The Mann and Kaimal turbulent wind field models have previously been found to predict significantly different global responses for some turbines. Godvik observed increased mooring line fatigue when applying the Mann model in simulations of the early Hywind 6 MW spar-type FWT design which is installed off of the coast of Scotland (10). The mooring system for the Hywind spar consists of three catenary lines, which are attached to the platform with a bridle (or delta) system in order to provide yaw stiffness. The main difference in mooring line response for the two wind coherence models was seen at low frequencies, and could be related to a difference in the low-frequency yaw response. Eliassen and Bachynski examined the differences in global motions and in mooring line fatigue for two semi-submersible wind turbines (11). Differences in the mooring line fatigue damage were also observed for the semi-submersibles: for low wind speeds, the Kaimal model resulted in larger surge motions and consequently larger mooring line load cycles, but the differences were less pronounced for higher wind speeds.

As mentioned earlier, the difference between the Kaimal and the Mann model is in the spatial structure of the generated wind field. Proper Orthogonal Decomposition (POD) is a statistical method to examine the coherent structures in turbulent flow (12). It yields an optimal decomposition of the turbulent flow into large coherent structures and it is optimal in terms of energy content for each mode (13). In combination with PIV measurements, POD can therefore be used to identify vortices (14, 15). For wind turbines, the wake behind the wind turbines has been studied using LES computations and POD has been applied to better understand the wake flow and make simplified models (16, 17). In the present study, the undisturbed turbulent flow field is of interest. The coherent structures in the generated wind field for wind turbines have also been investigated previously (18, 19). Saranyasoontorn related the coherent structures found in the POD analysis to the structural response of a small land-based wind turbine and found that only a few of the lowest POD modes were required to compute the low frequency energy in the wind turbine response (19). Eliassen studied the differences in the spatial coherence between the Kaimal and Mann model using POD, and shows that the two turbulence models differed in shape for the lowest POD modes. The Mann model had structures that were horizontally stretched relative to the Kaimal model (18).

The present work examines differences in response of three representative 5 MW FWTs (semi-submersible, spar, and TLP) when applying the Mann and Kaimal turbulent wind fields. The differences in the results are discussed with respect to a POD of the wind fields, which provides an intuitive explanation for why the coherence modelling can have important consequences for the global responses.

2 | TURBULENCE MODELS

The IEC design standard for wind turbines (7) recommends using the Kaimal wind spectrum for wind field modelling:

$$\frac{fS_k(f)}{\sigma_k^2} = 4\frac{\frac{fL_k}{U_{hub}}}{\left(1+6\frac{fL_k}{U_{hub}}\right)^{5/3}} \tag{1}$$

where f is the frequency in Hertz, $S_k(f)$ is the single-sided frequency spectrum, σ_k is the standard deviation of the velocity component, k is the index refering to the velocity direction, L_k integral scale component of the velocity and U_{hub} is the velocity at the hub height.

Both turbulence models, Kaimal and Mann, are using the Kaimal spectrum. However, the spatial distribution is different. The Kaimal model uses an exponential coherence function, where the coherence γ depends on the separation distance r and the frequency f:

$$\gamma(r,f) = \exp\left(12\left[\left(\frac{fr}{U_{hub}}\right)^2 + \left(\frac{0.12r}{L_c}\right)^2\right]^{0.5}\right) \tag{2}$$

where L_c is the coherence scale parameter ($L_c = 8.1\Lambda_1$ and Λ_1 is the turbulence scale parameter in meters, defined in the IEC standard (7)). The coherence is only applied to the longitudinal velocities and there is no coherence in the lateral nor in the vertical direction.

The Mann model is more complex, based on a combination of rapid distortion theory (RDT) with assumptions about the eddy lifetimes, and uses a velocity spectral tensor to describe the coherence in three dimensions (20). Compared to the Kaimal model, the Mann model has a more natural and more direct representation of the three-dimensional turbulent flow. In (21) it is shown how the Mann model can be fitted to the Kaimal spectrum and other measured wind spectra.

2.1 | Proper Orthogonal Decomposition (POD)

The POD method used in this study is based on Jørgensen et al (22). All three velocity components, $\boldsymbol{u} = (u, v, w)$, in longitudinal, lateral and vertical direction are considered. A study by Saranyasoontorn (19) used only the u-component to study loads on a small wind turbine, however the three-dimensionality of the wind is increasingly important for larger wind turbines. The velocity components, u, are first organized into N slices, one for each time-step:

$$\boldsymbol{U} = [\boldsymbol{u}_1 ... \boldsymbol{u}_N]. \tag{3}$$

For the wind fields used here, the number of points in the wind box is $32 \times 32 \times 40000$, where 32×32 are the spatial locations in the y-z plane, and there are 40000 spatial locations in x (alternatively these can be thought of as 40000 time steps). Each of these points has 3 velocity components (u, v, w). The length of each of the $N = 40000$ vectors $\boldsymbol{u}_i$ in Eq. 3 is therefore 3072 (by reorganizing the 32×32 points with 3 components (u, v, w) at each point). In our example, the size of matrix $\boldsymbol{U}$ is 3072×40000. The next step is to define the autocovariance matrix, $\boldsymbol{R}$, of the velocity matrix:

$$\boldsymbol{R} = \boldsymbol{U}^T\boldsymbol{U}. \tag{4}$$

The size of the matrix $\boldsymbol{R}$ is $N \times N$ (in our case, 40000×40000). The eigenvalues λ_i of the autocovariance matrix are collected in the eigenvalue matrix $\boldsymbol{\Lambda}$:

$$\boldsymbol{\Lambda} = \begin{bmatrix} \lambda_1 & & 0 \\ & \ddots & \\ 0 & & \lambda_N \end{bmatrix}. \tag{5}$$

Defining the corresponding orthonormal eigenvectors $\boldsymbol{g_i}$, of length N, and collecting them into a matrix $\boldsymbol{G} = [\boldsymbol{g_1 ... g_N}]$, such that

$$\boldsymbol{RG} = \boldsymbol{G\Lambda}, \tag{6}$$

the POD modes can now be defined as:

$$\phi_k = \frac{\boldsymbol{U}\boldsymbol{g}_j}{||\boldsymbol{U}\boldsymbol{g}_j||}. \tag{7}$$

The matrices $\mathbf{\Lambda}$ and $\boldsymbol{G}$ are each of size $N \times N$, in our case 40000×40000. Each of the POD modes is a vector of length equal to the number of rows in $\boldsymbol{U}$; here ϕ_k is 3072×1. The original wind velocity vector of slice j, $\boldsymbol{u}'_j$, can be reconstructed from the POD modes as:

$$\boldsymbol{u}'_j = \sum_{k=1}^{N} \phi_k a_{kj}, \tag{8}$$

where a_{kj} is a part of the $N \times N$ amplitude matrix $\boldsymbol{A}$:

$$\boldsymbol{A} = \mathbf{\Phi}^T \cdot \boldsymbol{U}. \tag{9}$$

In Eq. 9, the matrix $\mathbf{\Phi}$ contains the POD modes, giving it a size 3072×40000 in our example. The eigenvalue matrix, Λ, is the covariance matrix of $\boldsymbol{A}$, and the eigenvalues can be be used as a measure of the energy in each mode. The POD modes, which illustrate the spatial patterns that can be seen in the wind field, are sorted in terms of total kinetic energy content. Examples of the POD modes are shown among the results in Fig. 5 -8 . As with structural mode shapes, the magnitudes are normalized, and the sign (positive/negative) of the POD mode shape is only interesting in a relative sense. The higher modes are associated with lower energy levels, and a truncation of the higher modes can describe the random wind field reasonably accurately (19). An example of a short time series of wind speed at a grid point for the full wind field and for a reconstruction using a limited number of POD modes is shown in Fig. 1 . As shown, the first POD mode captures much of the low-frequency variation in the longitudinal wind speed.

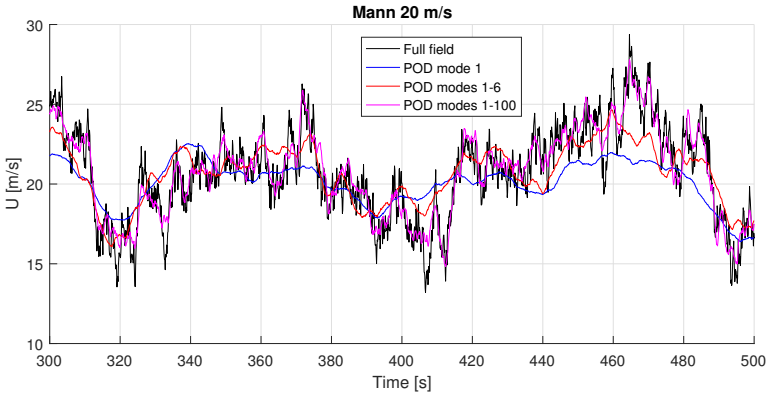

FIGURE 1 Time series of Mann 20 m/s wind field at a grid point near the hub, for the full field and selected POD modes.

The POD modes of a turbulent wind flow show the coherent structures, where coherent structures are defined as organized spatial features which repeatedly appear in the flow (12).

3 | FLOATING WIND TURBINE CONCEPTS AND MODELS

Three FWT concepts, each supporting the NREL 5 MW reference turbine (23), are considered in the present work: a semi-submersible, a spar, and a tension leg platform (TLP). Selected characteristics of the platforms are summarized in Table 1 , while additional details can be found in Sections 3.2-3.4 and the referenced literature therein.

The natural periods of the modelled FWTs, obtained by numerical decay tests in the SIMA simulation tool, are summarized in Table 2 . In all cases, the tower design differs from the reference 77.6 m tower in (24): the tower has been artificially softened in order to eliminate possible resonant excitation at the 3p frequency (0.34-0.6 Hz), which can occur due to the change in tower frequency which is seen on a floating support structure (25). Here, the softening is achieved by reducing the bending stiffness (EI) without changing the mass distribution. As such, the tower design is not entirely physical, but provides a reasonable model for global analysis.

TABLE 1 FWT characteristics.

	Semi-submersible [1]	Spar	TLP
Water depth (m)	320	320	150
Draft (m)	17	120	22
Displacement (tonnes)	4619	8227	5796
Platform pitch inertia about SWL (kg-m^2)	1.546×10^9	6.46×10^{10}	9.84×10^8
Platform yaw inertia about SWL (kg-m^2)	2.73×10^9	1.64×10^8	2.29×10^8

[1]Inertia given for neutral (no wind) ballast condition

TABLE 2 Natural periods in seconds based on numerical decay tests.

Mode	Semi-submersible	Spar	TLP
Surge	98.5	109.5	41.9
Heave	19.6	31.5	0.6
Pitch	37.7	29.2	3.27[1]
Yaw	64.5	7.3	18.6
First tower bending	3.31	3.32	0.41[2]

[1]Combined pitch/tower bending mode
[2]Second tower bending mode

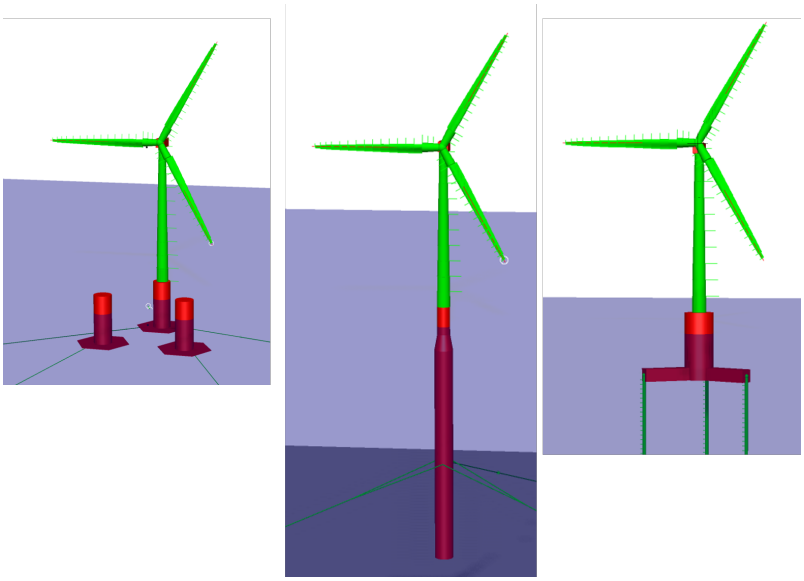

FIGURE 2 FWTs modelled in SIMA: semi-submersible, spar, and TLP.

All of the simulation models were built in the SIMA software from SINTEF Ocean, as illustrated in Fig. 2 , and the coordinate system and selected mooring lines for comparison are shown in Fig. 3 . Common characteristics of the numerical models are discussed in greater detail in Section 3.1, while design details and modelling considerations which are particular to the specific platforms are described in Sections 3.2-3.4.

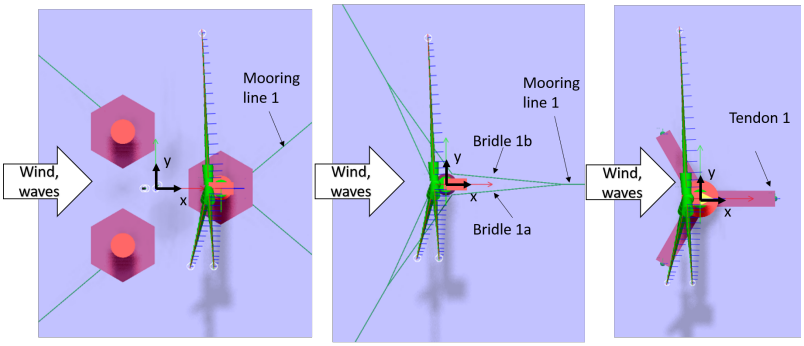

FIGURE 3 Coordinate systems and mooring line convention: semi-submersible, spar, and TLP.

3.1 | Load and response models

SIMA provides an aero-hydro-servo-elastic global modelling environment through the coupled RIFLEX-SIMO programs (26). The tower, blades, and mooring lines are modelled using nonlinear beam (or, for catenary lines, bar) elements, which can account for large rotations through a co-rotated formulation. The platform hull is modelled using a rigid body, which accounts for integrated hydrodynamic forces and moments according to linear potential flow theory. Viscous drag forces on the hull and on the mooring lines are modelled using the quadratic drag term in Morison's equation. Added mass on the mooring lines is also accounted for using Morison's equation.

Aerodynamic loads on the blades are computed using the Blade Element/Momentum (BEM) theory, including corrections for tip loss, dynamic stall, and dynamic wake effects. Drag forces on the tower and nacelle are not included in the simulations presented herein.

A simple lookup table controller for the generator torque and a proportional-integral controller for the blade pitch are included in the simulations. While the control logic follows the NREL 5 MW definition (23), the proportional (K_P) and integral (K_I) coefficients for the blade pitch controller were detuned to avoid negative feedback (27). Both the semi-submersible and spar use the control coefficients from (24) to avoid negative feedback near the pitch natural frequency, while the TLP is only detuned with respect to the main wave frequencies.

The numerical simulations are carried out using Newmark-beta time domain integration with time step 0.005 s. The numerical integration parameters ($1/\beta = 3.9$, $\gamma = 0.505$) are chosen to give a small numerical damping contribution.

3.2 | Semi-submersible

Semi-submersibles are characterized by their large waterplane moment of inertia, which provides stability without requiring the deep draft of a spar platform. The semi-submersible FWT is based on the generic 5 MW WindFloat concept (28) with the mooring system defined as in (29). A catenary mooring system with 4 lines provides the needed stiffness in surge, sway, and yaw.

The wind turbine is placed on one of the offset columns in the semi-submersible design. WindFloat has an active ballast system that counteracts the rotor's thrust force in order to maintain a mean platform pitch which is close to zero. The reaction time of this system is approximately 20 minutes (28). In the dynamic model, the ballast system was included by applying different mass and restoring matrices for each environmental condition, including the changed center of gravity and the change in inertia. The mass and restoring matrices were kept constant throughout each time domain simulation (no active changing of the ballast).

3.3 | Spar

Spar platforms are characterized by their large draft and small waterline area, and heavy ballast deep in the hull provides stability. The spar FWT in this study is based on the OC3-Hywind definition (24). In addition to the tower modifications which were previously discussed, the mooring system differed somewhat from the one which was applied in the OC3 project. Here, as in (25), the mooring system consisted of three catenary lines connected to the platform via delta (or bridle) lines. Clump weights

TABLE 3 Environmental conditions

U_{hub}	H_s (m)	T_p (s)	I
4	1.5	9.3	0.301
6	1.7	9.5	0.236
8	1.9	9.7	0.203
10	2.1	9.8	0.183
12	2.4	10.1	0.170
14	2.8	10.4	0.161
16	3.2	10.6	0.154
18	3.6	10.9	0.149
20	4.1	11.2	0.144
22	4.6	11.5	0.141
24	5.2	11.8	0.138

were also applied, giving the mooring system a similar effect on global stiffness as in (24). By modelling the mooring lines with bar elements, a full dynamic solution could be carried out, and the loads in both the single line and in the bridle were examined. Although this system is not exactly the same as the real Hywind design examined by Godvik (10), it has similar characteristics.

The spar buoy was modelled as a rigid body, and both first-order forces from linear potential theory and viscous hydrodynamic forces (using the drag coefficients as specified by Jonkman (24)) were included. Mean wave drift forces were applied and Newman's approximation was used to estimate the difference-frequency wave excitation.

3.4 | TLP

TLPs are characterized by their vertical pre-tensioned tendons which provide stability. The pretension makes the platform stiff in heave, roll, and pitch, while still compliant in surge, sway, and yaw motions. The TLP FWT design considered here corresponds to TLPWT #3 from (30), which is an approximately half-size version of the original Sea Star oil platform (31). Compared to other published TLP designs (eg (32),(33)), this design has relatively stiff and highly pre-tensioned tendons. The tendons were modelled using axis-symmetric beam elements, with hydrodynamic loads according to Morison's equation (with $C_a = 1$ and $C_d = 1$). Flex joints are modelled at the fairleads and at the otherwise rigid seabed, such that the connections can be described as pinned. For the hull, in addition to the first order and viscous forces, difference-frequency forces using Newman's approximation were also applied. Although second- and third-order forces may be important for the TLP responses (34, 35, 36), especially in large waves, these loads were not modelled in the present work, since the main focus is on the wind-induced responses.

4 | DYNAMIC ANALYSIS

4.1 | Environmental conditions

The dynamic analysis was carried out for a range of wind speeds where the turbine is operational. For each hub-height (90 m) wind speed (U_{hub}), the most likely significant wave height (H_s) and peak period (T_p) were selected according to the hindcast data for site 14 presented in (37). This site corresponds to a location offshore of the coast of Norway, with water depth 202 m and 50-year H_s 10.96 m. Despite the difference in water depth for the different platforms, the same environmental conditions were applied. The selected conditions in Table 3 were intended to span a range of realistic conditions - including waves, such that the results can be seen as representative - but do not correspond to a full set of conditions for fatigue analysis. Table 3 includes the turbulence intensity (I), which was selected based on the Normal Turbulence Model in the IEC standard (38), considering a Class B turbine.

For each environmental condition, six realizations of the wind and wave time series were generated. Each simulated realization had one hour duration (after transient). The wave elevation (with time step 0.1 s and frequency resolution 1.5×10^{-4} Hz) was

TABLE 4 Fatigue calculation parameters. D is the diameter, t is the thickness for circular cross sections.

Platform	Section	geometry	S-N curve
All	tower base, 10 m above SWL	$D = 6.5$ m, $t = 27$ mm	D in Table 2-1 (air), DNV-RP-C203 (45)
All	tower top, 87.6 m above SWL	$D = 3.87$ m, $t = 19$ mm	D in Table 2-1 (air), DNV-RP-C203 (45)
Semi	mooring at fairlead	equivalent $D = 7.5$ cm	studless chain in Table F1, DNV-OS-E301 (46)
TLP	tendon at fairlead	$D = 1.3$ m, $t = 42.9$ mm	F in Table 2-2 (seawater), DNV-RP-C203 (45)
Spar	mooring at bridle connection	equivalent $D = 9$ cm	studless chain in Table F1, DNV-OS-E301 (46)
Spar	bridle at fairlead	equivalent $D = 9$ cm	studless chain in Table F1, DNV-OS-E301 (46)

realized from a JONSWAP spectrum with the given H_s and T_p values, using the corresponding peak enhancement factor as in (39).

Three-dimensional wind fields were generated using the Mann 64-bit turbulence generator (40) (for the Mann model), and using the TurbSim tool from NREL (41) (for the Kaimal model). Both wind fields were read and interpolated in the same fashion, using identical spatial grids. The grid includes 32x32 points covering 160x160 m in the rotor plane with horizontal time step 0.1 s. A power law vertical wind speed profile with exponent 0.14 was applied (38). The same 6 wave realizations for each environmental condition were applied together with each type of simulated wind field, such that differences in response can be fully attributed to the wind field modelling.

4.2 | Fatigue calculation

In the present work, one-hour fatigue damage estimates for the tower base, tower top, and mooring lines were obtained from the global dynamic simulation results (time histories of loads at various cross sections). These loads are denoted N_x (axial force), V_y and V_z (shear forces), M_x (torsional moment), and M_y and M_z (bending moments). We focus on fatigue due to axial stress, since the fatigue due to shear stress is typically much smaller for similar structures (25).

For the tower sections as well as the tendons of the TLP, the axial stress σ_x at the outer radius r and angle θ in the local x-y plane on the hollow circular section is computed in the time domain as in Eq. 10.

$$\sigma_x = \frac{N_x}{A} + \frac{M_y}{I_y} r\sin(\theta) + \frac{M_z}{I_z} r\cos(\theta) \tag{10}$$

In Eq. 10, A represents cross-section area, while I_y and I_x are the cross-section's second moments of area calculated about the y and z axes, respectively. For the conditions considered here, with aligned wind and waves, the fatigue damage estimates for the tower are presented for a point on the cross section which is also aligned with the wind. After computing the time history of stress, the number of load cycles at different stress levels was counted using the rainflow counting technique for effective stress ranges (42). Here, we have used the implementation of rainflow cycle counting in WAFO (43). Finally, 1-hour fatigue damage (D_{RFC}) was estimated by assuming the Palmgren-Miner hypothesis (44):

$$D_{RFC} = \sum_{i=1}^{I} \frac{n_i}{N_i}, \tag{11}$$

where n_i is the number of cycles at a given stress level, and N_i is the number of cycles to failure at that stress level, given by an S-N curve. A small modification to the WAFO software was applied to allow for bilinear S-N curves for the tower and tendons. For the catenary chain mooring lines of the spar and semi-submersible and for the bridle lines of the spar, a similar procedure was used, but with $M_y = M_z = 0$. The section geometry and the S-N curves which were applied are summarized in Table 4 . Since the objective was to compare the estimates for different turbulent wind models, no stress concentration or safety factors were applied in the estimates. All presented damage estimates are based on the average of six one-hour estimates.

5 | RESULTS AND DISCUSSION

5.1 | Wind fields

Fig. 4 shows the obtained standard deviation of the longitudinal wind speed (σ_u) and longitudinal wind spectra (S_u) compared to the prescribed values from the standards (7). Results are extracted at a grid point near the hub: due to the even number of grid points, there is no grid point exactly at the hub. The turbulence intensity at the hub is slightly lower than the presented results, due to averaging among neighboring grid points.

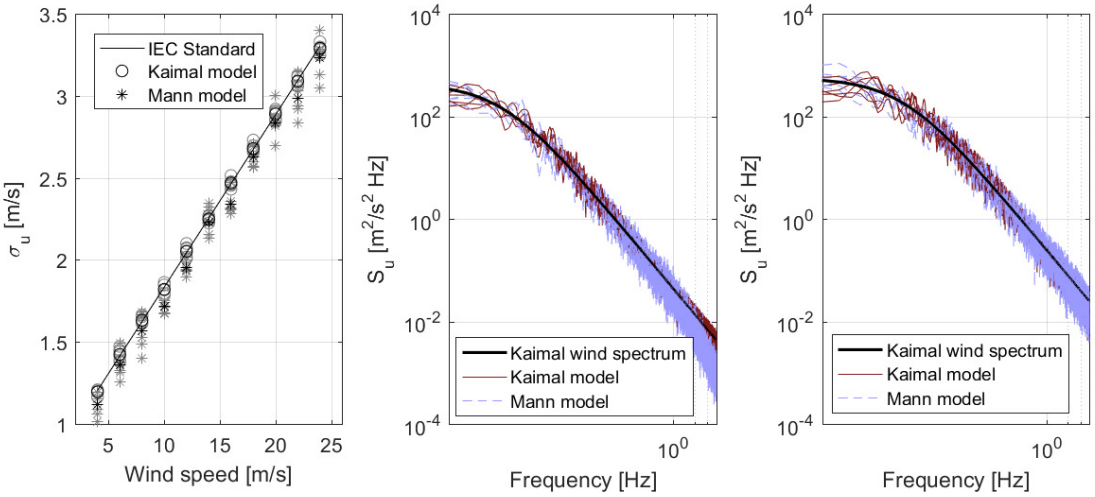

FIGURE 4 Left: standard deviation of longitudinal wind speed at a grid point near the hub. Darker markers show the average of 6 1-hour realizations, while lighter markers show individual realizations. Middle and right: turbulence spectra for 8 m/s and 20 m/s wind speeds, respectively. 6 1-hour realizations of each turbulence model are shown together with the theoretical spectrum.

The results in Fig. 4 show the expected variations in time domain realizations and generally follow the prescribed inputs. The obtained turbulence intensity for the Mann model is typically slightly lower than that of the Kaimal model.

The first six POD modes for 3-hour realizations of the wind field at 8 m/s and at 20 m/s are shown in Figs. 5 and 7 for the Kaimal model, and in Figs. 6 and 8 for the Mann model. A single wind field realization for each wind speed/turbulence model combination is shown: these results are representative of the patterns seen for other realizations, although there are variations in the details of the mode shapes. The colors represent the POD mode shape, ϕ_k (Eq 7), in the longitudinal (U) direction. The POD modes show the spatial patterns that can be observed in the wind field, and the lowest POD modes contain the most energy. The black circle in each subfigure represents the area of the rotor within the wind field.

A few features of the POD modes are interesting to note:

- For both models, the first POD mode (the most energetic mode) consists of single major coherent structure. This feature is typically more uniform across the rotor disk and centered for the Kaimal model compared to the Mann model.
- As one moves towards higher modes, there are more (and smaller) important coherent features in the pattern. By the sixth mode, one can generally see four peaks and valleys.
- At higher wind speeds, the features become more clearly defined.
- The Mann model tends to have smoother contours, while the Kaimal model does not have equally well-defined features.
- The coherent structures found in the higher POD modes tend to come in pairs with opposing diagonal symmetry which passes through the center of the rotor for the Kaimal model. For the Mann model the coherent structures often have some symmetry about a horizontal or vertical line (which is not necessarily centered about the rotor center).

The presence of such differences in the coherent structures in the POD modes is a natural consequence of the differences in the generation of the wind fields. Visualizing these modes is a useful way to interpret the differences in the response of FWTs. Note that the vertical and transverse components of the mode shapes are not shown in Figs. 5 -8 . There is no similar pattern in the POD mode shapes for these components in the Kaimal model. In the Mann model, the pattern seen in the longitudinal direction (U) is also visible (with opposite sign) in the vertical direction (W) (see (18)).

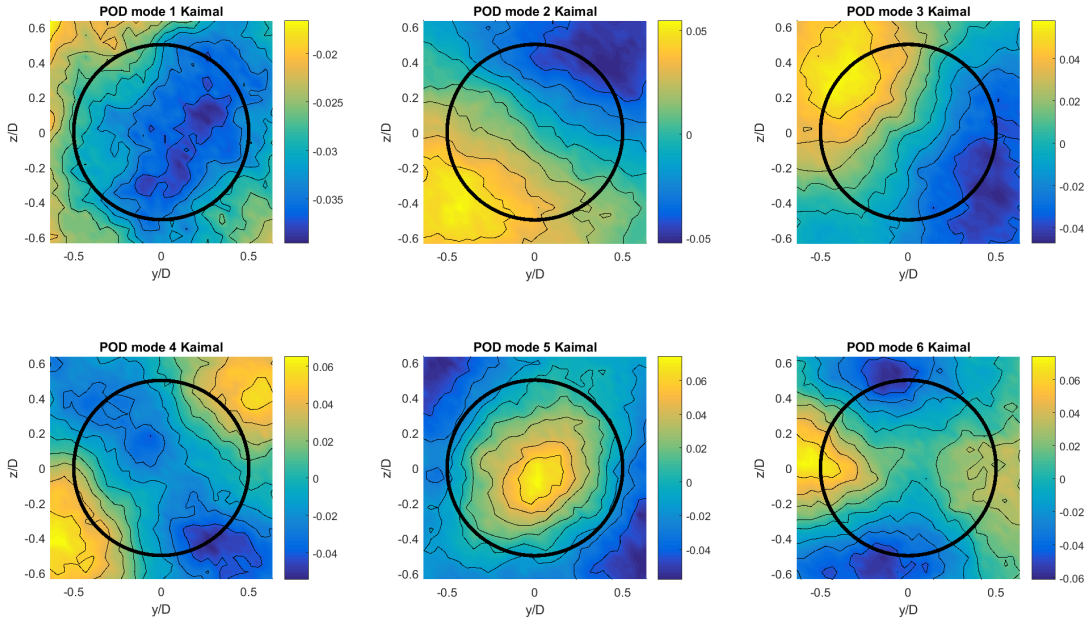

FIGURE 5 First 6 POD modes (longitudinal direction, normalized), Kaimal model, $U = 8$ m/s. The black circle represents the area of the rotor within the wind field.

The cumulative energy content in the first 100 POD modes (out of 3072 non-zero modes in the present simulations) was obtained from the eigenvalues and is shown in Fig. 9 . Consistent with the findings in (18), the first mode contributed roughly 20 % of the total energy for both models, while subsequent modes had smaller contributions. Beyond the first mode, the Mann model had more energy concentrated in lower modes compared to the Kaimal model, as shown in the right side of Fig. 9 .

As previously shown in Fig. 1 , the first POD mode captures much of the low-frequency variation in the longitudinal wind speed. To illustrate the contributions to the wind field obtained with the first six modes, Figs. 10 -12 show integration of the horizontal wind speed over the rotor based on the reconstruction of the turbulent wind from individual modes. Results for 20 m/s are shown; results for 8 m/s are generally similar to the presented results.

Fig. 10 shows the spectral density of the unweighted integration of the longitudinal reconstructed turbulent wind speed, $\int\int u' \mathrm{d}y\mathrm{d}z$, where u' is the longitudinal component of $\boldsymbol{u'}$ from Eq. 8, and the integration is carried out over the rotor plane area. As exemplified for the 20 m/s wind field, the integration of the first mode is much larger than any of the other contributions. The Kaimal model tends to give a larger integrated wind speed due to the first mode, especially around the surge natural frequency for the representative platforms studied here. There is, of course, significant variation among realizations of the wind field, and there are modes where the Mann model has a larger contribution, but the overall integration suggests that the Kaimal model should give larger surge (and platform pitch) excitation.

Fig. 11 shows the weighted integration of the longitudinal reconstructed wind speed, $\int\int u' z \mathrm{d}y\mathrm{d}z$, which illustrates the "pitching" moment of the wind field. While the first mode has a relatively small contribution, the second POD mode in the Mann model has a very large contribution. This is in good agreement with the pattern shown in Fig. 8 , and a similar pattern can be seen in all of the realizations of the Mann wind field for both 8 m/s and 20 m/s. Due to variations among realizations,

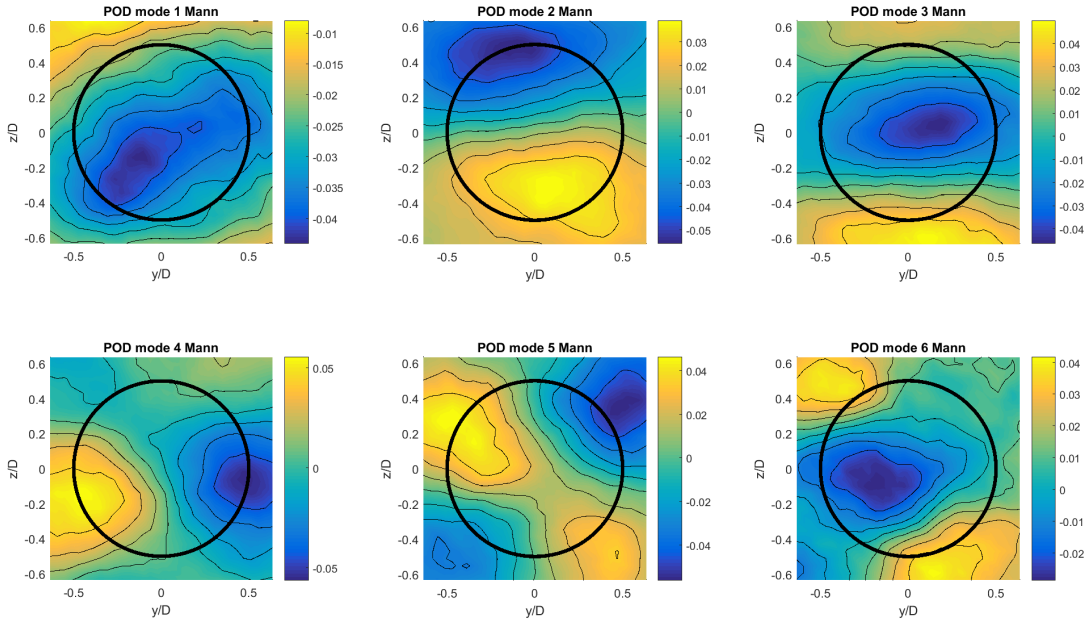

FIGURE 6 First 6 POD modes (longitudinal direction, normalized), Mann model, $U = 8$ m/s. The black circle represents the area of the rotor within the wind field.

the weighted “pitching" integration varies significantly for higher modes, but these modes have relatively small contributions in the range of frequencies of interest.

Fig. 12 shows the weighted integration of the longitudinal reconstructed wind speed, $\int\int u' y \mathrm{d}y\mathrm{d}z$, which illustrates the “yawing” moment of the wind field. The first POD mode has a small contribution, while the second and third modes for the Kaimal model tend to have relatively large contributions. The fourth and fifth modes for the Mann model contribute nearly as much as the second and third Kaimal modes, and tend to remain higher over the range of frequencies from 0.01 Hz to 0.1 Hz.

For comparison, the integration of the full turbulent wind field is shown in Fig. 13 . The unweighted integration highlights the large “surging" contribution of the Kaimal wind field, while the “pitching" moment of the Mann wind field is generally larger for frequencies below 0.1 Hz (due to the 2nd POD mode). For the “yawing" moment of the total wind field, there is no systematic difference between the two wind models, despite the significant differences in individual POD modes. It should be noted that the present integration is not necessarily representative of the loads on the turbine, which also include effects from, for example, induction and variations in the chord length along the blades, which are not included in this very simple integration of the wind speed itself.

5.2 | Global motions

Fig. 14 shows the standard deviation (σ) of the global motions of all three platforms for the different environmental conditions. The subscripts 1-6 represent surge, sway, heave, roll, pitch, and yaw, respectively. Each data point represents the average standard deviation from six 1-hour simulations of a given environmental condition (Table 3), which is identified by the mean wind speed at the hub. The surge and pitch standard deviations roughly followed the shape of the mean thrust curve, except for the TLP whose surge standard deviation was more closely related to the standard deviation in the incoming wind.

There were clear differences in the responses depending on which turbulence model was employed in the input. The Kaimal model gave larger responses in surge and pitch, while the Mann model showed significantly larger yaw responses. This is consistent with previous observations (10, 11). Sway and roll motions were small compared to the corresponding surge and pitch motions for low wind speeds, but increased with increasing wind speed. The sway and roll motions tended to be slightly larger for the Mann model than for the Kaimal model. The heave motion was primarily linked to wave loads for the semi-submersible

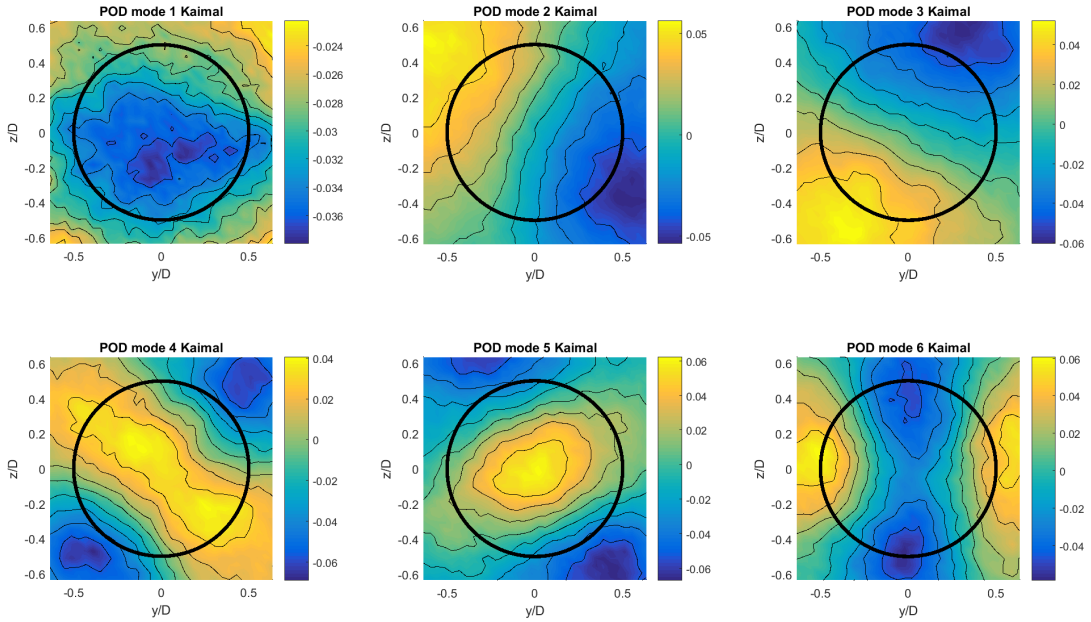

FIGURE 7 First 6 POD modes (longitudinal direction, normalized), Kaimal model, $U = 20$ m/s. The black circle represents the area of the rotor within the wind field.

and for the TLP. Due to its shape, the wave-induced loads on the spar are small and the heave motion (which is reported at the still water level) for this platform, unlike the others, includes some non-negligible components at low frequencies. Most of these motions are in reality due to the pitch and roll motions about a point far below the waterline. The differences between the two models in heave can be related to the roll and pitch motions: for moderate wind speeds, the pitch motions (larger with the Kaimal model) dominate, while for larger wind speeds, the roll motions (larger with the Mann model) dominate. All three platforms showed similar tendencies regarding the changes in standard deviation of the global motions as a function of the turbulence model, despite significant differences in their characteristics. The mechanisms which lead to differences in the global motions in surge, pitch, yaw, roll, and sway are discussed in greater detail in the subsequent paragraphs. The heave motion, which is either wave-dominated or simply related to the rotations, is not discussed further. All of the trends with respect to low-frequency responses were also observed in simulations without waves, however, these results are not presented here.

As illustrated in Fig. 15 for 20 m/s wind speed, the surge response at the platform natural frequencies in surge and in pitch, as well as the quasi-static response at even lower frequencies, was most sensitive to the turbulent wind field model, and these responses were consistently larger for the Kaimal model. As expected, the wave frequency response was independent of the turbulence model, and there was little global motion in response to wind-induced loads at higher frequencies. Similar results could be seen for different environmental conditions (not shown), with the very low-frequency quasi-static response typically dominating for lower wind speeds, and the surge natural period becoming more important for higher wind speeds. Due to the low natural frequency in surge for all of the platforms, there is no significant response at frequencies above the wave frequencies.

The surge results exemplified in Fig. 15 can be qualitatively related to the first POD mode shown in Figs. 7 and 8 . The first POD mode, which contains a large proportion of the energy in the turbulent wind field, was relatively uniform over the majority of the rotor, especially for the Kaimal model. A strong spatially uniform but time-varying flow can be expected to result in large thrust variations, and small out-of-plane forcing. The subsequent Kaimal mode “pairs" also contribute to a more uniform forcing over the rotor disk, which can contribute to significant surge motions.

Similar to the surge response, the platform pitch response at low frequencies and at the platform natural frequencies (in pitch and surge) was consistently higher when the Kaimal turbulence model was applied. Fig. 16 illustrates typical responses for 14 m/s wind speed. Note that, as expected, the pitch responses of the TLP were several orders of magnitude smaller than those of the spar and semi-submersible. Based on the POD modes with symmetry about a horizontal line (i.e. mode 2 in Figs. 6 and

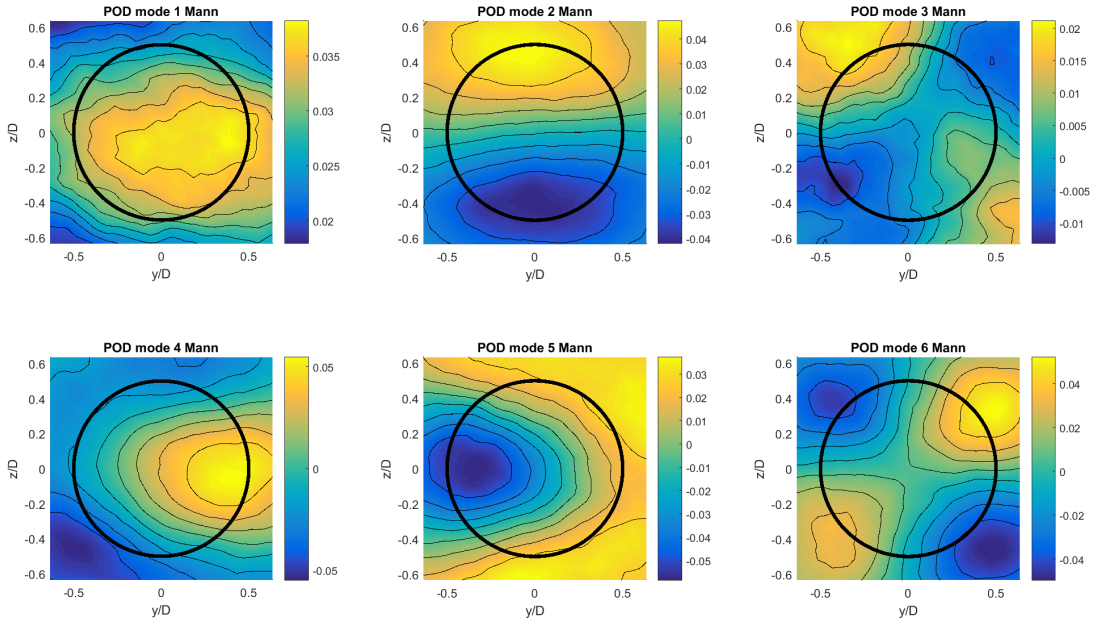

FIGURE 8 First 6 POD modes (longitudinal direction, normalized), Mann model, $U = 20$ m/s. The black circle represents the area of the rotor within the wind field.

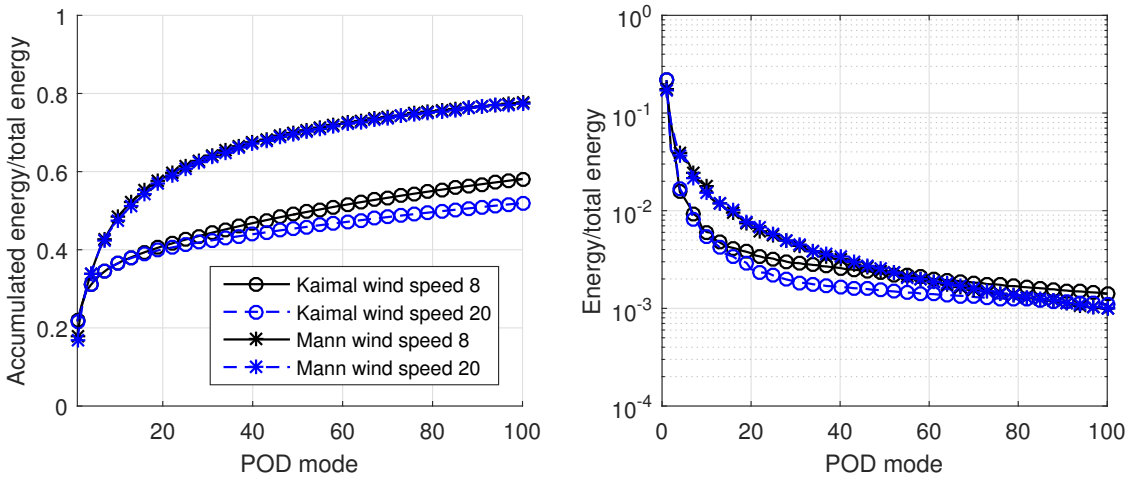

FIGURE 9 Left: cumulative energy content in the POD modes. Right: energy content in the POD modes.

8) and the integration shown in Figs. 11 and 13 , a larger local pitching moment about the hub would be expected for the Mann model, but the larger pitch response for the Kaimal model is consistent with the fact that the global pitching moment is dominated by the thrust force rather than the local pitching moment at the hub (see also (47)).

The yaw response, shown in Fig. 17 for wind speeds 8 m/s and 20 m/s, was consistently higher when the Mann turbulence model was applied, but there were differences in how the platforms behaved. The semi-submersible, which has a relatively soft mooring and large moment of inertia in yaw, responded primarily at its natural frequency. The spar, which has the highest mooring stiffness and lowest moment of inertia in yaw, responded primarily quasi-statically at low frequencies. The spar model also showed some response at the rotor frequency (1p). Because this response is not seen in constant wind/still water conditions,

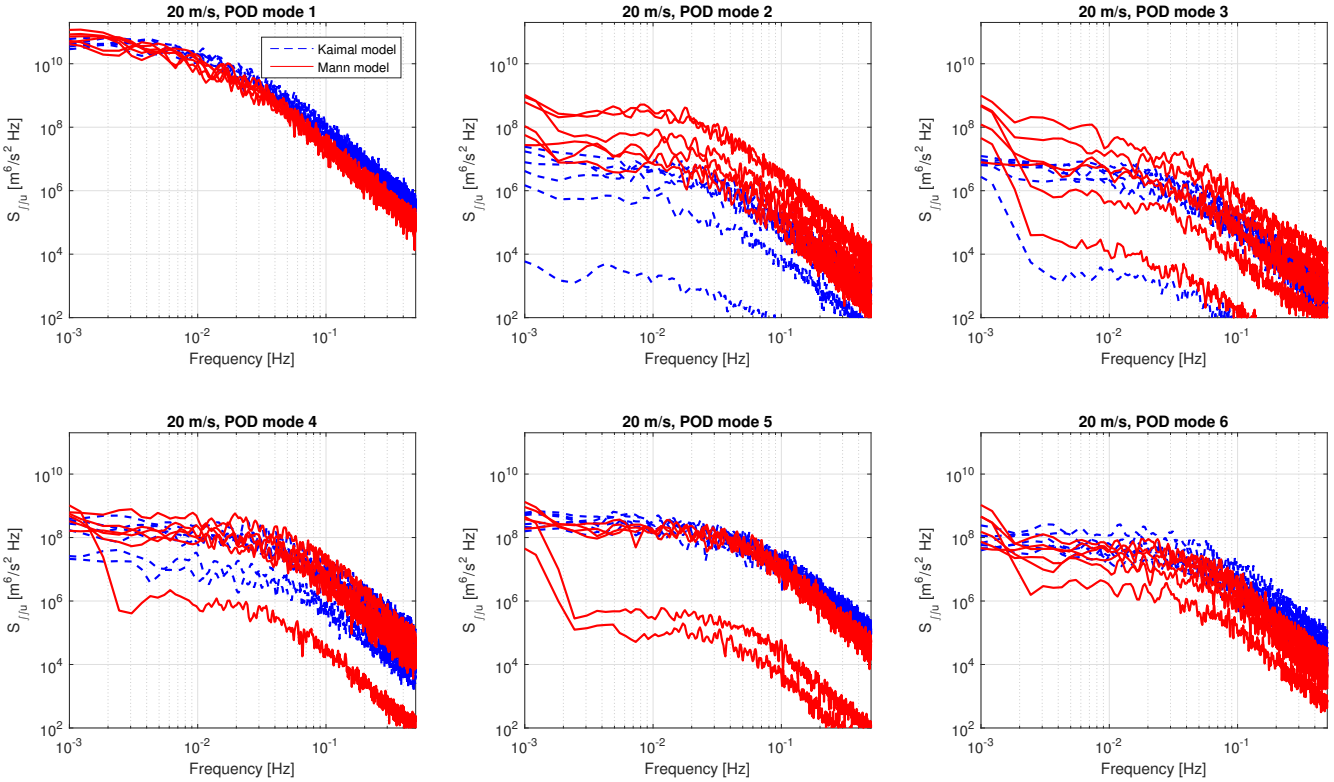

FIGURE 10 Power spectral density of the unweighted integration of the longitudinal reconstructed wind speed for individual POD modes, wind speed 20 m/s.

but it is seen in the aerodynamic yaw moment in simulations of the isolated NREL 5 MW rotor under turbulent wind conditions (especially for higher wind speeds), this 1p response is understood to be primarily related to turbulence sampling. Due to the proximity of the 1p frequency and the spar natural frequency in yaw, there was a non-negligible response, whereas the other platforms did not respond strongly at that frequency.

The connection between the larger low-frequency yaw response when applying the Mann model and the large, asymmetric mode shapes with uneven forcing on the right and left side of the rotor in the Mann model (e.g. modes 4 and 6 in Fig. 6 and modes 4 and 5 in Fig. 8) is discussed in greater detail in Section 5.4.

Although the mean motions in sway and roll were much smaller than the corresponding surge and pitch, the standard deviation of these motions at high wind speeds could take on similar magnitudes (as shown in Fig. 14). The sway and roll responses were closely connected, and only the roll motions are illustrated for a single case in Fig. 18 . Both the sway and roll natural frequencies can be seen in the sway and roll motions of the spar and semi-submersible, while the TLP sway and roll motions (which are very small in roll) were primarily concentrated at the sway and yaw natural frequencies. There was negligible wave-frequency response in sway and roll, as expected. The larger sway and roll responses when applying the Mann model are understood in a similar manner to the yaw motions: the non-uniformity of the wind field across the rotor results in a yaw moment (which in turn results in yaw motion and a thrust force which is not aligned with the mean wind direction) as well as a larger sideways force component (which can be seen in simulations with an isolated rotor).

5.3 | Tower, mooring line and bridle responses

In addition to the global motions, the wind field model also had consequences for the loads in components such as the tower and mooring lines of FWTs. Fig. 19 shows the estimated 1-hour fatigue damage at the tower base, tower top, downwind mooring line (see Table 4) and the bridle of the spar for different wind speeds.

The tower base fatigue damage was not very sensitive to the choice of turbulent wind model. As shown in Fig. 20 , the bending moment at the tower base (which was the dominant contributor to axial stress) depended strongly on the wave-frequency loading.

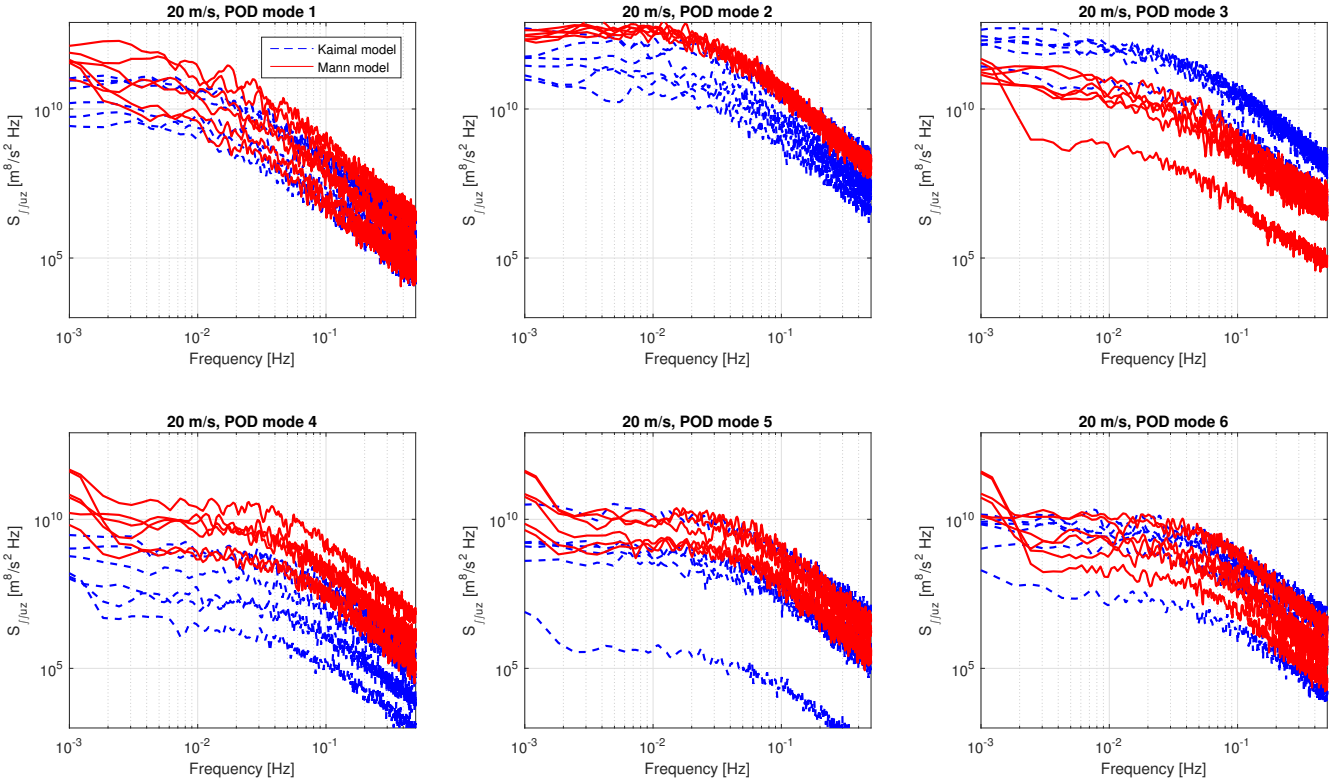

FIGURE 11 Power spectral density of the z-weighted integration of the longitudinal reconstructed wind speed for individual POD modes (pitching moment), wind speed 20 m/s.

Although there were peaks at the low-frequency resonance frequencies, particularly in pitch for the semi-submersible and spar, as well as some quasi-static response at very low frequencies, these contributed a low number of cycles and lower stress range variation than the wave-induced variations. The Kaimal model gave slightly larger fatigue damage for the spar, especially for relatively high wind speeds, but there was no clear pattern for the other platforms.

At the tower top, as shown in Fig. 21 , the wave-induced variations in the bending moment were relatively small. Low-frequency (quasi-static) variations in the bending moment followed the incoming wind spectrum, and the load variation at the 3p frequency was also important. For the spar, there were tower top fore-aft bending moment variations at the 1p frequency as well. The load variation at the 3p frequency was consistently higher for the Mann model than for the Kaimal model, which resulted in consistently higher fatigue damage estimates for the semi-submersible and TLP models. For the spar, the tower top fatigue damage depended on the relative contribution at 1p (typically larger for the Kaimal model) compared to the 3p load variation. For the environmental conditions in the range 18-20 m/s, the 1p contribution dominated, but otherwise the 3p variation was more important. The tower top bending moment and fatigue effects highlight the fact that the differences between the two models were not limited to the low-frequency effects which were important for the platform motions and the mooring line responses.

Fig. 22 shows the power density spectra of the downwind mooring lines and bridle tension for two wind speeds. The catenary mooring lines for the semi-submersible and spar are designed to primarily take up low-frequency loads, and the dominant response is seen at the surge (or sway) natural frequency. For low wind speeds, where the surge motions were dominant, the Kaimal model gave larger response and larger damage. For higher wind speeds, as the sway motions became more important, the Mann model gave larger response and larger damage estimates in some cases.

The TLP tendons take up both the low-frequency and the wave-frequency loads. For low wind speeds, the wave-frequency contribution was dominant and there was little difference in the fatigue damage predicted by the two models. For higher wind speeds, the damage prediction for the TLP tendons using Mann's wind field model was larger due to the larger response at the first pitch/bending natural frequency.

The largest and most consistent difference between the two models was related to the bridle fatigue damage for the spar. Compared to the Kaimal model, the simulations with the Mann model predicted up to twice as much fatigue damage in the

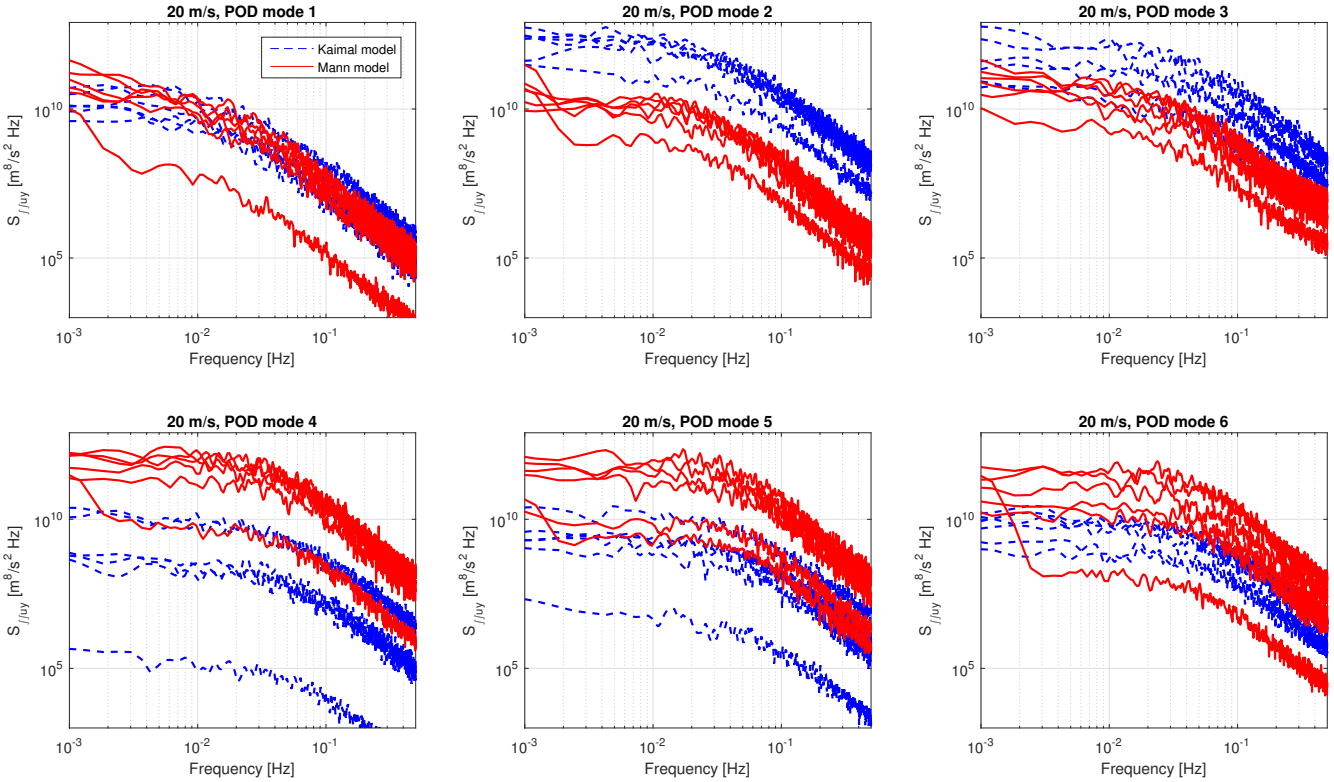

FIGURE 12 Power spectral density of the y-weighted integration of the longitudinal reconstructed wind speed for individual POD modes (yawing moment), wind speed 20 m/s.

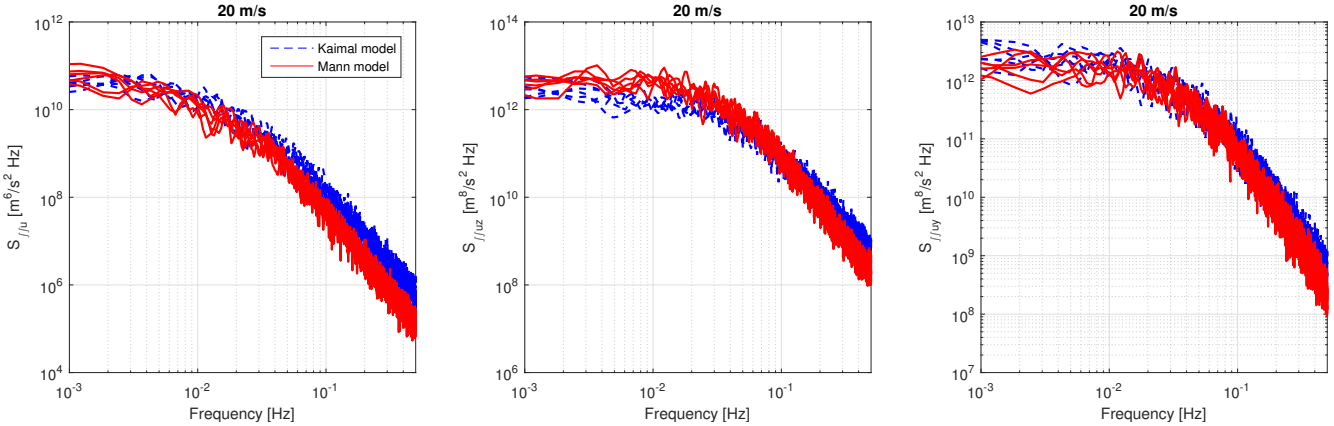

FIGURE 13 Power spectral density of the unweighted (left), z-weighted (middle), and y-weighted (right) integration of the longitudinal reconstructed wind speed, wind speed 20 m/s.

bridle for high wind speeds. Below rated, the difference was smaller, but there was still a significant and consistent difference between the models. The comparison of the tension spectra in Fig. 22 shows that the bridle response at low frequencies was higher when the Mann model was applied. Peaks in the spectrum related to the surge and pitch motions can be seen, but the difference is understood to be primarily related to the quasi-static yaw motion.

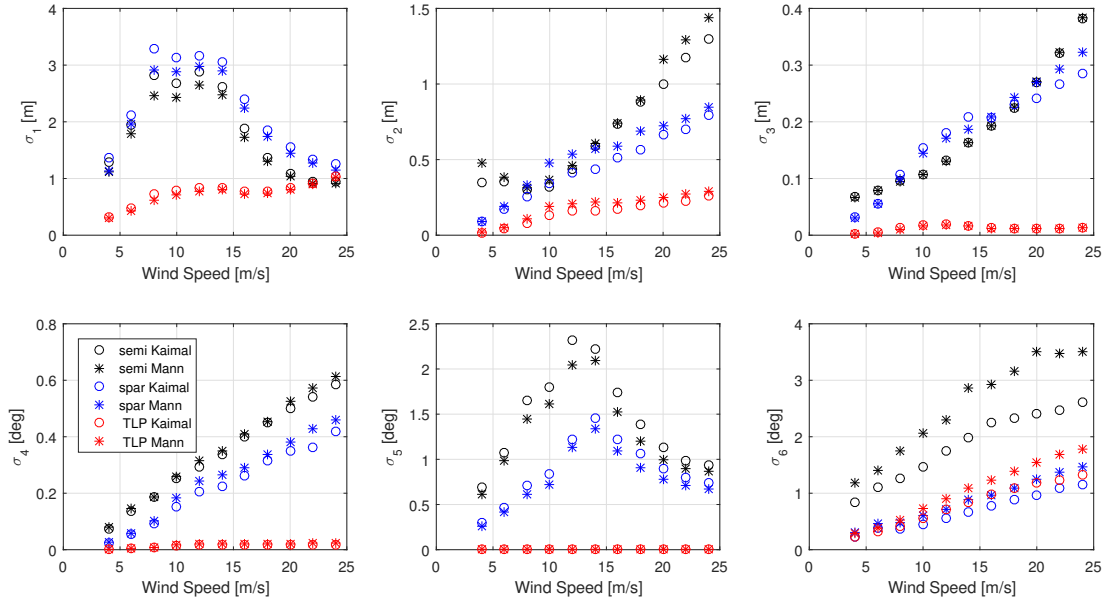

FIGURE 14 Standard deviations of global motions, average of six 1-hour simulations for each environmental condition

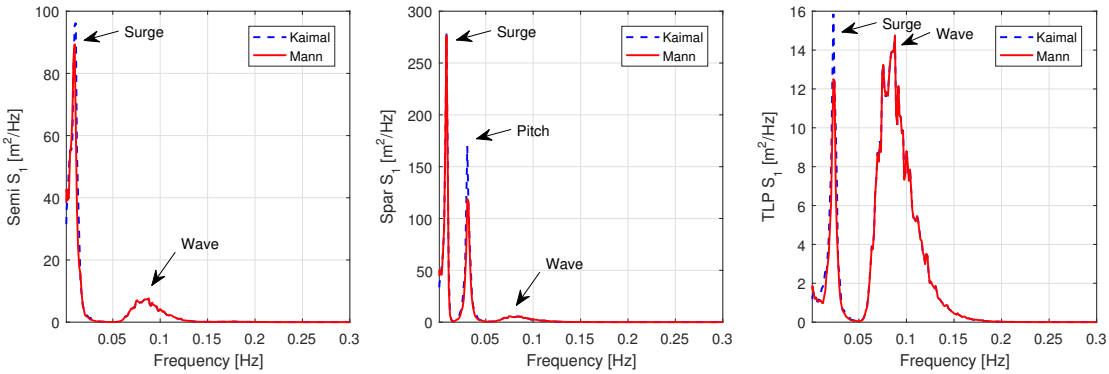

FIGURE 15 Platform surge response, wind speed 20 m/s

5.4 | Responses to reconstructed wind fields

In order to better relate the obtained results with the POD modes in the wind, the 8 m/s and 20 m/s wind fields were recreated with a limited number of POD modes: only mode 1, only modes 1-6, and only modes 1-100. It should be noted that there are differences in the energy contained in a given number of modes for each model (see Fig. 9), but that these differences are most pronounced for larger numbers of modes. Global analysis simulations were then carried out with these recreated wind fields and the same wave realizations as the the simulations with the complete wind field. As in the previous simulations, 6 one-hour simulations were carried out for each condition. The resulting standard deviation of surge motion and of yaw motion for all three platforms are shown in Figs. 23 and 24 , respectively.

Fig. 23 shows that the first POD mode in the wind field was sufficient for capturing the majority of the response in surge. As shown in Fig. 15 , the majority of the surge response was at very low frequencies or at the wave frequency. It is reasonable to expect the first POD mode to capture the majority of this response due to its large low-frequency contribution, and due to the fact that the mode shape is typically unidirectional and uniform across the rotor disk. The wave-frequency response was unaffected by the wind field.

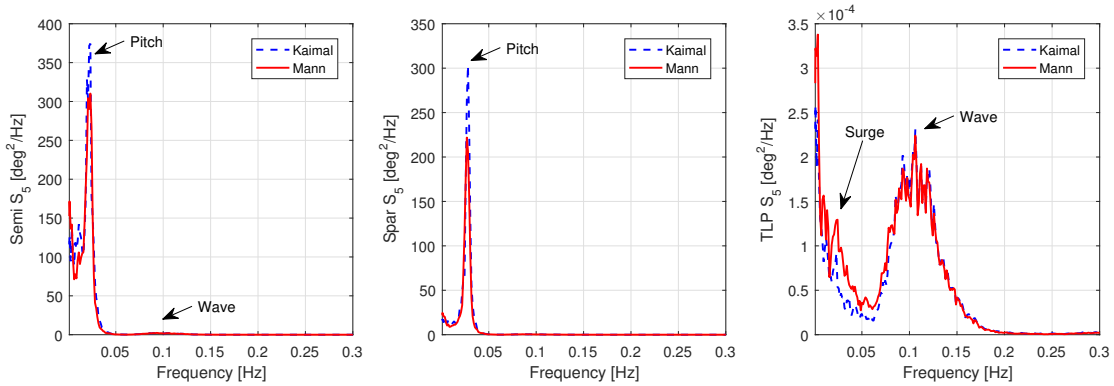

FIGURE 16 Platform pitch response, wind speed 14 m/s

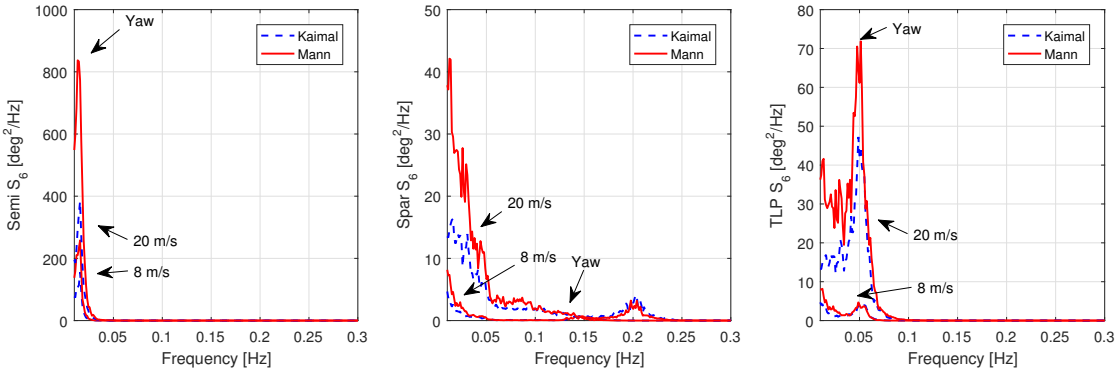

FIGURE 17 Platform yaw response, wind speeds 8 m/s and 20 m/s

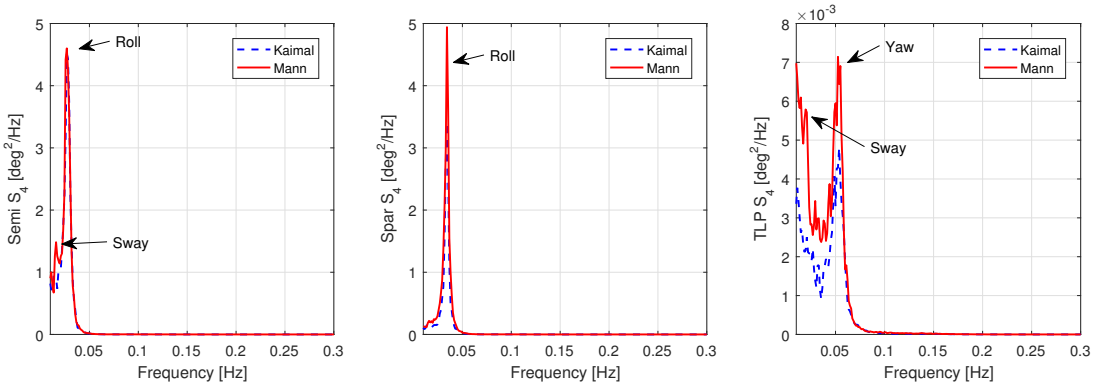

FIGURE 18 Platform roll response, wind speed 10 m/s

The pitch response (not shown), like the surge response, was almost completely captured with only the first POD mode, while the yaw response in Fig. 24 was almost zero for the first mode. The first 6 POD modes were, however, sufficient to capture the majority of the yaw response.

Fig. 25 shows the frequency distribution of the yaw response depending on the number of POD modes for the 20 m/s wind speed. As shown, the first POD mode gave very little yaw response. Qualitatively, the yaw response to the reconstructed wind fields is easily related to the mode shapes shown previously: the first mode is quite uniform across the rotor disk and leads to little yaw loading. Adding the second and third mode for the Kaimal model and the fourth and fifth mode for the Mann model

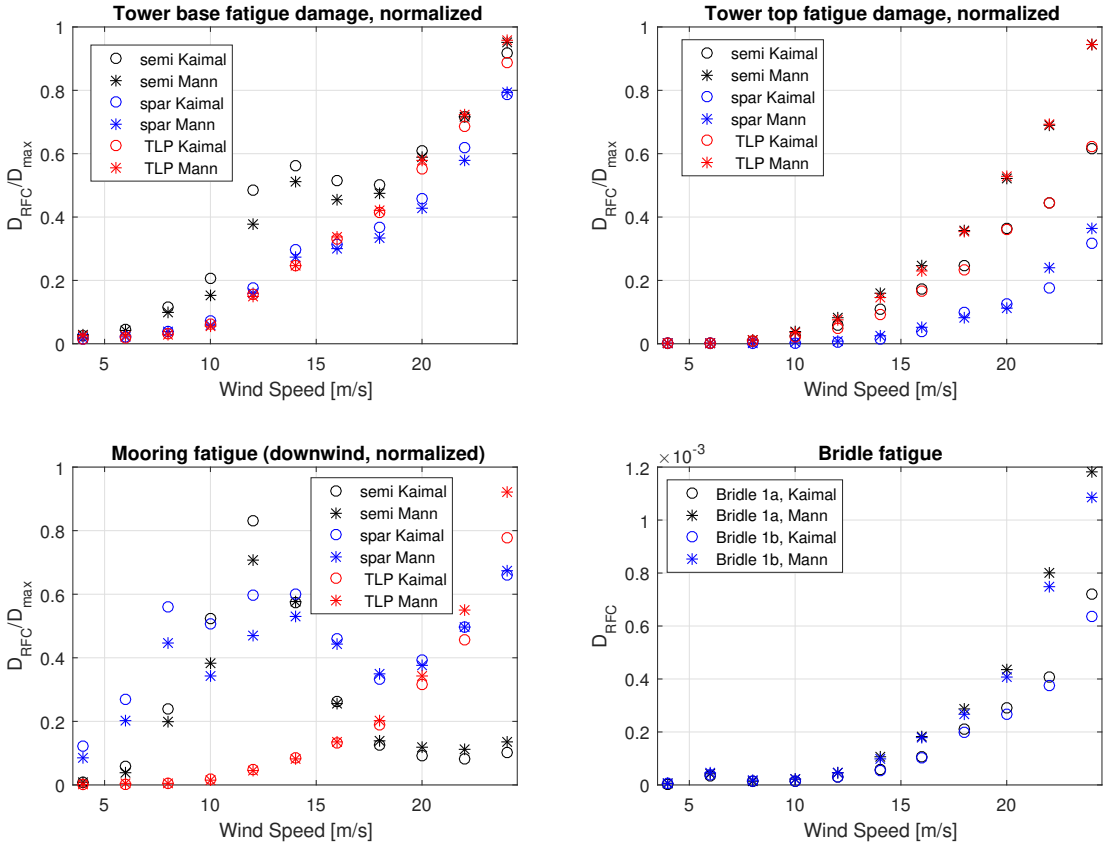

FIGURE 19 Estimated 1-hour fatigue damage (averaged over 6 seeds) for the tower base, tower top, mooring line (or tendon) 1 and the bridle of the spar mooring system. Note that the mooring and tower fatigue damage are normalized by the maximum 1-hour (one seed) damage for each platform. The normalized tower top fatigue damage for the semi and TLP with the Mann model largely overlaps.

gives a significant increase in the yaw response. The lower modes capture the majority of the low-frequency response, while adding the rest of the POD modes up to 100 brings the response at higher frequencies closer to the full field response.

The results for the sway and roll standard deviation were similar to the yaw motions: little response was captured by a single POD mode, while the majority of the response - including the main differences in response between the Mann and Kaimal models - was captured when the first 6 modes were included.

The bending moments at the tower base and tower top, as well as the mooring line tension, from the simulations with the reconstructed wind fields showed consistent results with respect to the motions. Fatigue damage was not calculated, but standard deviations were considered. The standard deviation of the tower base bending moment, which is dominated by the wave loads and by pitch and surge motions, was well captured (within 6 %) with a single POD mode. The standard deviation of the tower top bending moment, on the other hand, was not very well captured by either 1 or 6 POD modes in the reconstructed wind field. Higher POD modes were needed in order to capture the variations near the 3p frequency. With 100 POD modes, the standard deviation of the tower top bending moment was within 3 % of the result with the full wind field.

As shown in Fig. 26 , the standard deviation of the mooring line tension for the catenary-moored platforms was well captured by the first POD mode, while the TLP tendon tension required higher modes to reach a similar level of response as the simulations with the full wind field. For the bridle line of the spar, the difference between the Mann and Kaimal models was visible based on the first six POD modes. This is consistent with the observations of the yaw motion, but the bridle tensions were more sensitive to slightly higher frequencies (within the low-frequency range, around 0.03 Hz) than the platform motions.

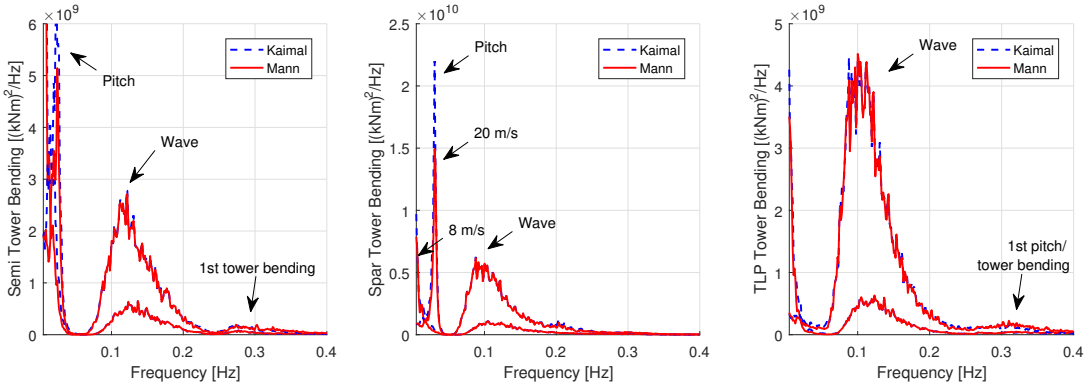

FIGURE 20 Tower base bending moment, wind speed 8 m/s and 20 m/s

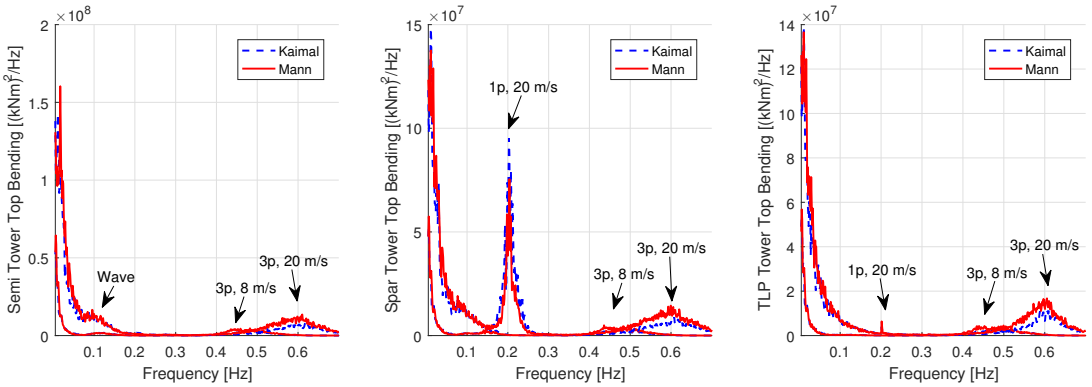

FIGURE 21 Tower top bending moment, wind speed 8 m/s and 20 m/s

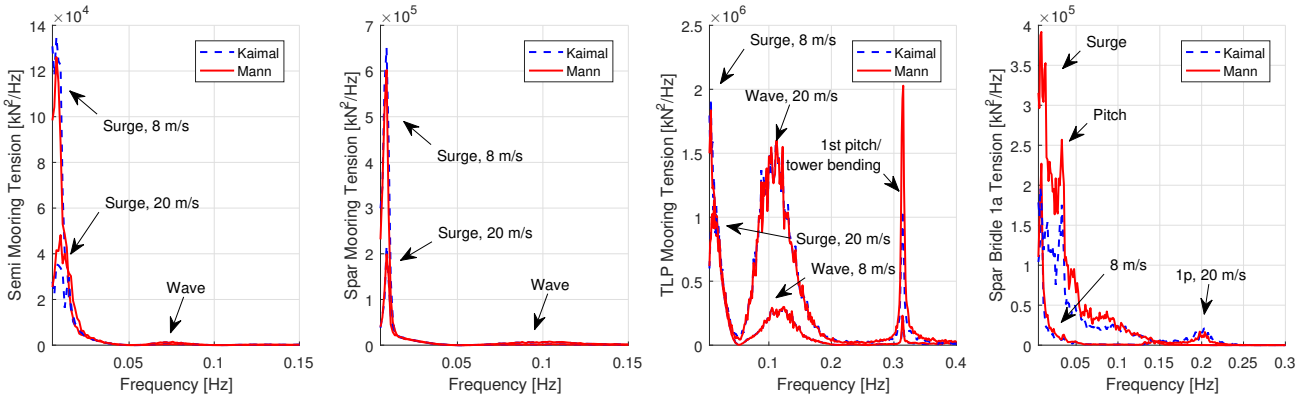

FIGURE 22 Mooring line 1 tension for the semi, spar and TLP, and bridle 1a tension, wind speed 8 m/s and 20 m/s. Note that frequency ranges differ for each subplot in order to include the important responses.

6 | CONCLUSIONS

The effect of the spatial coherence in the turbulent wind field on the global responses of three representative 5 MW floating wind turbines (semi-submersible, spar, and TLP) has been investigated in the present work. Numerical simulations using an aero-hydro-servo-elastic tool (considering beam elements and rigid bodies to model the structure, a combination of potential flow and semi-empirical viscous forces for the hydrodynamics, blade element/momentum theory aerodynamics, and a reference

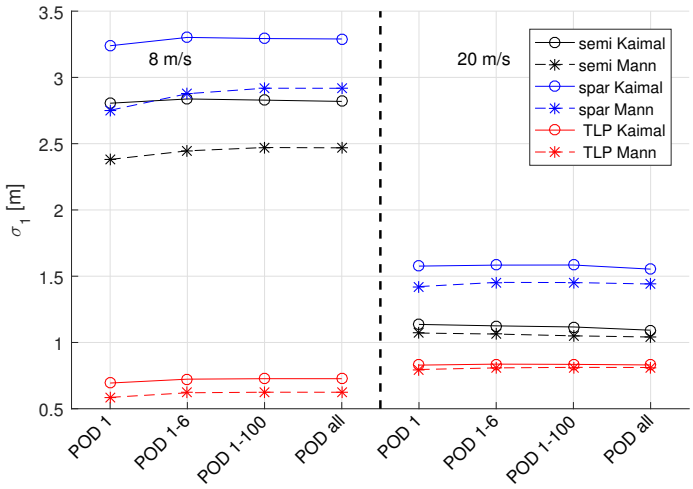

FIGURE 23 Platform surge response standard deviation, depending on number of POD modes in the incoming wind field. “POD all" refers to the original wind field.

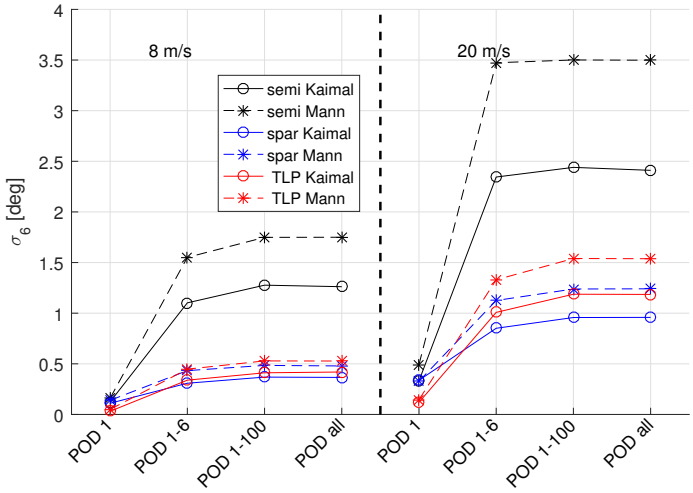

FIGURE 24 Platform yaw response standard deviation, depending on number of POD modes in the incoming wind field. “POD all" refers to the original wind field.

variable speed pitch control system) were carried out considering two types of turbulent wind field. The “Kaimal" wind field considers exponential coherence in the longitudinal direction, and no coherence in the lateral or vertical directions. The “Mann" wind field model uses a velocity spectral tensor, and includes three-dimensional coherence.

The most important differences in the floating wind turbine global motion responses were in the low-frequency (lower than the wave frequency) range. The Kaimal model consistently resulted in larger surge and pitch responses, while the Mann model resulted in larger yaw, sway, and roll. The differences in response were strongest for the softest platforms: 5-20 % higher surge standard deviation for the spar with the Kaimal wind model and 30-40 % higher yaw standard deviation for the semi with the Mann wind model. These differences make some intuitive sense: the coherent structures which differ between the two wind field models are associated with long time scales, such that they are most important for responses which are sensitive to long time scales. Differences were nonetheless large for other platforms - the surge motion of the TLP was 2-10 % higher with the Kaimal wind, and the spar and TLP both experienced 20-30 % larger yaw standard deviation with the Mann model.

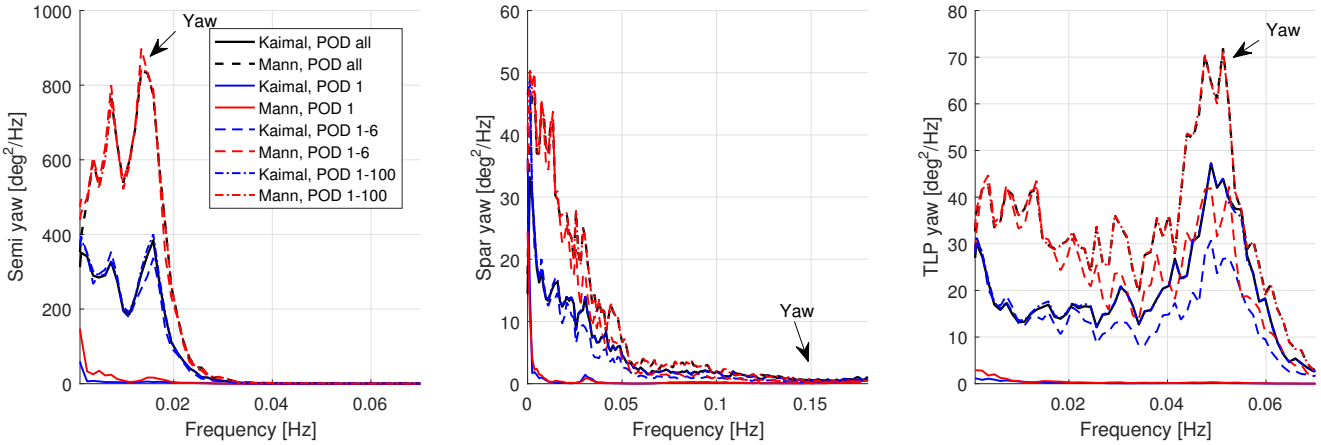

FIGURE 25 Yaw response spectra, 20 m/s wind speed, depending on number of POD modes in the incoming wind field. “POD all" refers to the original wind field. Note that the spar response is extended to a wider frequency range.

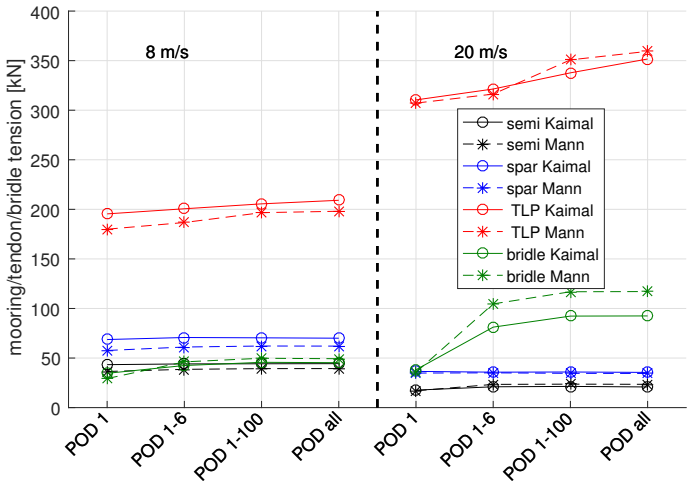

FIGURE 26 Standard deviation of the mooring line, tendon, and bridle tension response, depending on number of POD modes in the incoming wind field. “POD all" refers to the original wind field.

The loads in the tower and mooring system also depended on the spatial coherence model in the wind field. Stresses and fatigue in the tower base were primarily determined by the wave excitation, but the tower top fatigue damage depended strongly on the 3p excitation, which tended to be larger for the Mann model. The mooring line fatigue was closely related to the global motions. For the semi-submersible and spar platforms, the low-frequency surge responses were important for the mooring line stresses, and the simulations with the Kaimal model gave significantly larger (20-25 %) fatigue damage predictions. The bridle line of the spar mooring system was particularly sensitive to the yaw response, and fatigue damage according to simulations with the Mann model could be twice as large.

Proper orthogonal decomposition techniques were used to visualize the different features of the two types of wind fields, and reconstructed wind fields with a limited number of POD modes were used to better understand the differences in the wind fields. The majority of the surge and pitch response could be related to the first POD mode. The majority of the differences in the yaw responses between the two wind types was seen through the first 6 POD modes.

The present work does not examine the question of which wind field model is more correct - such a study would require extensive measurement data - but rather focuses on the different results which can be obtained by using standard methods

from the industry. Compared to bottom-fixed offshore wind turbines, floating wind turbines are more sensitive to low-frequency variations in the flow across the rotor, and the present results, as well as several preceding studies, suggest that a new focus on wind modelling is needed in order to increase the reliability of global analysis tools for these structures. The observations from the present work could be used to suggest the eddy size and patterns which might be relevant for data collection and analysis related to further development of engineering models for the wind field used in floating wind turbine global analysis.

ACKNOWLEDGMENTS

The second author acknowledges financial support through the DIMSELO project (NFR grant 228865). Søren Andersen's implementation of the POD was adopted with few changes, and his contribution is gratefully acknowledged.

References

[1] Cordle A, Jonkman J. State of the Art in Floating Wind Turbine Design Tools. In: Twenty-first (2011) International Offshore and Polar Engineering Conference, vol. 1: :367-374; 2011.

[2] Jonkman J, Butterfield S, Passon P, et al. Offshore Code Comparison Collaboration within IEA Wind Annex XXIII: Phase II Results Regarding Monopile Foundation Modeling. In: IEA European Offshore Wind Conference; 2007; Berlin, Germany.

[3] Robertson A, Jonkman J, Musial W, Vorpahl F, Popko W. Offshore Code Comparison Collaboration, Continuation: Phase II Results of a Floating Semisubmersible Wind System. In: no. NREL/CP-5000-60600 in EWEA Offshore; 2013.

[4] Tucker MJ, Challenor PG, Carter DJT. Numerical simulation of a random sea: a common error and its effect upon wave group statistics. *Applied Ocean Research.* 1984;6(2):118 - 122.

[5] Det Norske Veritas . *Design of Floating Wind Turbine Structures.* DNV-OS-J103: ; 2013.

[6] American Bureau of Shipping . *Guide for building and classing floating offshore wind turbine installations.* : ; 2013.

[7] International Electrotechnical Commission (IEC) . *Wind turbines: Part 1: Design Requirements.* IEC61400-1:2005: ; 2005.

[8] Dimitrov N, Natarajan A, Mann J. Effects of normal and extreme turbulence spectral parameters on wind turbine loads. *Renewable Energy.* 2017;101:1180 - 1193.

[9] Eliassen Lene, Obhrai Charlotte. Coherence of Turbulent Wind Under Neutral Wind Conditions at FINO1. *Energy Procedia.* 2016;94(Supplement C):388 - 398. 13th Deep Sea Offshore Wind R&D Conference, EERA DeepWind'2016.

[10] Godvik M. Influence of the wind coherence on the response of a floating wind turbine ,. In: Science meets Industry; 2016; Stavanger.

[11] Eliassen L, Bachynski EE. The effect of turbulence modelling on the response of a large floating wind turbine. In: no. OMAE2017-61179 in ASME 2017 36th International Conference on Ocean, Offshore and Arctic Engineering; 2017; Trondheim, Norway.

[12] Berkooz Gal, Holmes Philip, Lumley John L. The proper orthogonal decomposition in the analysis of turbulent flows. *Annual review of fluid mechanics.* 1993;25(1):539–575.

[13] Andersen Søren Juhl, Sørensen Jens Nørkær, Mikkelsen Robert. Reduced order model of the inherent turbulence of wind turbine wakes inside an infinitely long row of turbines. In: :012005IOP Publishing; 2014.

[14] Jensch M, Brede M, Leder A, Frederich O, Thiele F. Use of proper orthogonal decomposition to visualize coherent structures from time resolved PIV data. In: Proceedings of the 14th Int. Symp. on Applications of Laser Techniques to Fluid Mechanics:07–10; 2008.

[15] Graftieaux L, Michard M, Grosjean N. Combining PIV, POD and vortex identification algorithms for the study of unsteady turbulent swirling flows. *Measurement Science and technology.* 2001;12(9):1422.

[16] Bastine D, Witha B, Wächter M, Peinke J. POD analysis of a wind turbine wake in a turbulent atmospheric boundary layer. In: Journal of Physics: Conference Series, vol. 524: :012153IOP Publishing; 2014.

[17] Andersen SJ, Sørensen JN, Mikkelsen R. Simulation of the inherent turbulence and wake interaction inside an infinitely long row of wind turbines. *Journal of Turbulence.* 2013;14(4):1–24.

[18] Eliassen L, Andersen S. Investigating Coherent Structures in the Standard Turbulence Models using Proper Orthogonal Decomposition. *Journal of Physics: Conference Series.* 2016;753.

[19] Saranyasoontorn K, Manuel L. Low-Dimensional Representations of Inflow Turbulence and Wind Turbine Response Using Proper Orthogonal Decomposition. *Journal of Solar Energy Engineering.* 2005;127(4):553-562.

[20] Mann Jakob. The spatial structure of neutral atmospheric surface-layer turbulence. *Journal of fluid mechanics.* 1994;273:141–168.

[21] Mann J. Wind field simulation. *Probabilistic Engineering Mechanics.* 1998;13(4):269-282.

[22] Jørgensen BH, Sørensen JN, Brøns M. Low-dimensional modeling of a driven cavity flow with two free parameters. *Theoretical and computational fluid dynamics.* 2003;16(4):299–317.

[23] Jonkman J, Butterfield S, Musial W, Scott G. *Definition of a 5-MW Reference Wind Turbine for Offshore System Development.* NREL/TP-500-38060: National Renewable Energy Laboratory; 2009.

[24] Jonkman J. *Definition of the Floating System for Phase IV of OC3.* NREL/TLP-500-47535: ; 2010.

[25] Bachynski EE, Kvittem MI, Luan C, Moan T. Wind-wave misalignment effects on floating wind turbines: motions and tower load effects. *Journal of Offshore Mechanics and Arctic Engineering.* 2014;136:041902-1–041902-12.

[26] Ormberg H, Bachynski EE. Global analysis of floating wind turbines: Code development, model sensitivity and benchmark study. In: 22nd International Offshore and Polar Engineering Conference, vol. 1: :366-373; 2012.

[27] Larsen TJ, Hanson TD. A method to avoid negative damped low frequent tower vibrations for a floating, pitch controlled wind turbine. *Journal of Physics: Conference Series, The Second Conference on The Science of Making Torque from Wind.* 2007;75.

[28] Roddier D, Peiffer A, Aubault A, Weinstein J. A Generic 5 MW WindFloat for Numerical Tool Validation & Comparison against a Generic Spar. In: no. OMAE2011-50278 in 30th International Conference on Ocean, Offshore and Arctic Engineering; 2011.

[29] Kvittem MI. Modelling and response analysis for fatigue design of a semi-submersible wind turbine. PhD thesisNorwegian University of Science and Technology2014.

[30] Bachynski EE, Moan T. Design Considerations for Tension Leg Platform Wind Turbines. *Marine Structures.* 2012;29:89-114.

[31] Kibbee SE, Leverette SJ, Davies KB, Matten RB. Morpeth SeaStar Mini-TLP. In: no. OTC 10855 in Offshore Technology Conference; 1999.

[32] Matha D, Fischer T, Kuhn M, Jonkman J. Model Development and Loads Analysis of a Wind Turbine on a Floating Offshore Tension Leg Platform. In: no. NREL/CP-500-46725; 2010.

[33] Stewart G, Lackner M, Robertson A, Jonkman J, Goupee A. Calibration and Validation of a FAST Floating Wind Turbine Model of the DeepCwind Scaled Tension-Leg Platform. In: 22nd International Offshore and Polar Engineering Conference, vol. 1: :380-387; 2012.

[34] Roald L, Jonkman J, Robertson A, Chokani N. Effect of Second-Order Hydrodynamics on Floating Offshore Wind Turbines. *Energy Procedia.* 2013;35:253-264.

[35] Bachynski EE, Moan T. Ringing Loads on Tension Leg Platform Wind Turbines. *Ocean Engineering.* 2014;84:237-248.

[36] Bae YH, Kim MH. Turbine-floater-tether coupled dynamic analysis including second-order sum-frequency wave loads for a TLP-type FOWT (floating offshore wind turbine). In: no. OMAE2013-11261 in 32nd International Conference on Ocean, Offshore and Arctic Engineering; 2013.

[37] Li L, Gao Z, Moan T. Joint Environmental Data at Five European Offshore Sites for Design of Combined Wind and Wave Energy Concepts. In: no. OMAE2013-10156 in 32nd International Conference on Ocean, Offshore, and Arctic Engineering; 2013.

[38] International Electrotechnical Commission (IEC) . *Wind turbines: Part 3: Design requirements for offshore wind turbines.* IEC61400-3: ; 2009.

[39] Det Norske Veritas . *Environmental Conditions and Environmental Loads.* DNV-RP-C205: ; 2010.

[40] DTU Wind Energy . *Pre-processing tools - HAWC2.* : ; 2014.

[41] Jonkman BJ. *TurbSim User's Guide: Version 1.50.* NREL/TP-500-46198: National Renewable Energy Laboratory; 2009.

[42] Matsuishi M, Endo T. Fatigue of metals subjected to varying stress.. In: Proceedings of the Kyushu Branch of Japan Society of Mechanics Engineering:37-40; 1968.

[43] Brodtkorb PA, Johannesson P, Lindgren G, Rychlik I, Rydén J, Sjö E. WAFO - a MATLAB Toolbox for the Analysis of Random Waves and Loads. In: Proc. 10th Int. Offshore and Polar Eng. Conf., ISOPE, Seattle, USA, vol. 3: :343–350International Society of Offshore and Polar Engineers; 2000.

[44] Naess A, Moan T. *Stochastic Dynamics of Marine Structures*. Cambridge University Press; 2013.

[45] Det Norske Veritas . *Fatigue Design of Offshore Steel Structures.* DNV-RP-C203: ; 2010.

[46] Det Norske Veritas . *Position Mooring.* DNV-OS-E301: ; 2010.

[47] Bachynski Erin E., Chabaud Valentin, Sauder Thomas. Real-time hybrid model testing of floating wind turbines: sensitivity to limited actuation. *Energy Procedia.* 2015;80:2-12.

How cite this article: Bachynski, E.E. and L. Eliassen (2017), XX, *Wind Energy*, *2017;00:1–6*.